

# Direct visualization of Rashba-split bands and spin/orbital-charge interconversion at $\text{KTaO}_3$ interfaces

Received: 12 May 2022

Accepted: 23 September 2022

Published online: 18 October 2022

Check for updates

Sara Varotto<sup>1,6</sup>, Annika Johansson<sup>2,6</sup>✉, Börge Göbel<sup>3,6</sup>, Luis M. Vicente-Arche<sup>1</sup>, Srijani Mallik<sup>1</sup>, Julien Bréhin<sup>1</sup>, Raphaël Salazar<sup>4</sup>, François Bertran<sup>4</sup>, Patrick Le Fèvre<sup>4</sup>, Nicolas Bergeal<sup>5</sup>, Julien Rault<sup>4</sup>, Ingrid Mertig<sup>3</sup> & Manuel Bibes<sup>1</sup>✉

Rashba interfaces have emerged as promising platforms for spin-charge interconversion through the direct and inverse Edelstein effects. Notably, oxide-based two-dimensional electron gases display a large and gate-tunable conversion efficiency, as determined by transport measurements. However, a direct visualization of the Rashba-split bands in oxide two-dimensional electron gases is lacking, which hampers an advanced understanding of their rich spin-orbit physics. Here, we investigate  $\text{KTaO}_3$  two-dimensional electron gases and evidence their Rashba-split bands using angle resolved photoemission spectroscopy. Fitting the bands with a tight-binding Hamiltonian, we extract the effective Rashba coefficient and bring insight into the complex multi-orbital nature of the band structure. Our calculations reveal unconventional spin and orbital textures, showing compensation effects from quasi-degenerate band pairs which strongly depend on in-plane anisotropy. We compute the band-resolved spin and orbital Edelstein effects, and predict interconversion efficiencies exceeding those of other oxide two-dimensional electron gases. Finally, we suggest design rules for Rashba systems to optimize spin-charge interconversion performance.

The Rashba effect is a manifestation of spin-orbit coupling occurring in systems with broken inversion symmetry<sup>1</sup>. In its simplest form, the Rashba spin-orbit coupling (RSOC) acts on a spin-degenerate pair of parabolic bands by shifting each band oppositely along the wavevector  $\mathbf{k}$ , depending on the spin direction<sup>2</sup> (with an energy splitting linear in  $k$ ). A constant energy cut of the band structure then shows two concentric circular Fermi contours on which the spins of the electronic states are tangential (and thus locked perpendicular to  $\mathbf{k}$ ), curling clockwise for one contour and counter-clockwise for the other.

The first direct visualization of Rashba-split bands using angle-resolved photoemission spectroscopy (ARPES) was reported at the surface of heavy metals such as Au<sup>3,4</sup> or of their alloys<sup>5</sup> where the RSOC coefficient  $\alpha_R$  can take values in the range of a few eV · Å. The spin-momentum locking of Rashba systems was later harnessed to interconvert spin and charge currents (direct and inverse Rashba–Edelstein effects) at interfaces between heavy metals<sup>6</sup> and also in oxide-based two-dimensional electron gases (2DEGs)<sup>7,8</sup>. Just a few years after their discovery<sup>9</sup>, a finite RSOC was indeed

<sup>1</sup>Unité Mixte de Physique, CNRS, Thales, Université Paris-Saclay, 91767 Palaiseau, France. <sup>2</sup>Max Planck Institute of Microstructure Physics, Weinberg 2, 06120 Halle, Germany. <sup>3</sup>Institute of Physics, Martin-Luther-Universität Halle-Wittenberg, 06099 Halle, Germany. <sup>4</sup>Synchrotron SOLEIL, L'Orme des Merisiers, Saint-Aubin, BP 48, Gif-sur-Yvette Cedex 91192, France. <sup>5</sup>Laboratoire de Physique et d'Etude des Matériaux, ESPCI Paris, Université PSL, CNRS, 75005 Paris, France. <sup>6</sup>These authors contributed equally: Sara Varotto, Annika Johansson, Börge Göbel. ✉ e-mail: [annika.johansson@mpi-halle.mpg.de](mailto:annika.johansson@mpi-halle.mpg.de); [manuel.bibes@cnrs-thales.fr](mailto:manuel.bibes@cnrs-thales.fr)

identified through weak antilocalization (WAL) in  $\text{LaAlO}_3/\text{SrTiO}_3$  (LAO/STO) 2DEGs<sup>10</sup>, which are non-centrosymmetric systems.  $\alpha_R$  was found to amount to a few tens of  $\text{meV}\cdot\text{\AA}$ —considerably lower than at the surface of heavy metals—and, quite remarkably, to be tuneable by a gate voltage<sup>10,11</sup>. Aside from a report of a giant RSOC at the surface of STO<sup>12</sup> that later studies did not observe<sup>13</sup>, ARPES could not provide a direct visualization of Rashba-split bands in STO 2DEGs due to the limitation in the energy resolution. This moderate  $\alpha_R$  combined with the long scattering time of such 2DEGs was however successfully used to achieve spin-charge interconversion with very high efficiency<sup>7,8</sup>.

Another family of oxide 2DEGs is based on  $\text{KTaO}_3$  (KTO) instead of STO<sup>14</sup>. Bulk STO and KTO share several features: they are both quantum paraelectrics and become n-type conductors when doped with minute amounts of impurities<sup>15</sup>. Just like STO, KTO may also harbor 2DEGs when interfaced with appropriate materials such as LAO<sup>16</sup>,  $\text{LaVO}_3$ <sup>17</sup> or reactive metals such as Al (that locally create oxygen vacancies which are n-type dopants)<sup>18</sup>. One major difference though is that Ta is much heavier than Ti and thus RSOC in KTO 2DEGs should be significantly stronger than in STO 2DEGs. Indeed, WAL data yields  $\alpha_R \approx 300 \text{ meV}\cdot\text{\AA}$ <sup>16</sup> and compatible values were recently derived from bilinear magnetoresistance experiments<sup>18</sup>. Despite several attempts to use ARPES to map the band structure of KTO 2DEGs<sup>19,20</sup>, Rashba-split bands were nonetheless never observed, although band structure calculations on KTO<sup>16</sup> and related systems<sup>21</sup> do predict a strong Rashba splitting of the Ta  $d_{xz/yz}$  bands. Therefore, the band structure of (001)-oriented KTO 2DEGs remains elusive to this day, as is the direct visualization of Rashba splitting in any oxide, except for surface states in delafossite single crystals<sup>22</sup>.

In this paper, we report the synthesis of (001)-oriented KTO 2DEGs through the deposition of 1  $\text{\AA}$  of Al by molecular beam epitaxy. We use ARPES to measure the band dispersion and associated Fermi surfaces. The data reveal a pair of Rashba-split  $d_{xz/yz}$  bands with a  $\alpha_R$  consistent with values extracted from magnetotransport<sup>16,18</sup> and earlier density-functional theory (DFT) calculations<sup>16</sup>. We fit the ARPES data with an 14-band tight-binding (TB) Hamiltonian (see Methods), determine the corresponding spin and orbital textures and compute the Edelstein effect for each

band pair. We finally discuss the role of symmetry and anisotropy on the Edelstein effect.

## Results

### Band structure of KTO(001) 2DEGs

To create an electron gas in a (001)-oriented single crystal of KTO, we deposited 1–2  $\text{\AA}$  of Al by molecular beam epitaxy (MBE) following the same protocol as detailed in refs. 18, 23. The sample was then transferred in ultra high vacuum to the ARPES measurement chamber (see Methods). Figure 1 displays the detailed band structure of KTO//Al(1  $\text{\AA}$ ) near  $\Gamma_{002}$  (corresponding to a photon energy of 31 eV at normal emission). Results from 2  $\text{\AA}$  samples gave very similar results, albeit with a poorer signal to noise ratio. We observed a metallic state at the surface, with nearly parabolic bands crossing the Fermi level  $\epsilon_F$ . By varying the photon energy we found that the probed states did not significantly disperse with  $k_z$ , thereby confirming the quasi-2D nature of the electron gas. In Fig. 1a, we show the band dispersion along the (100) in-plane direction with linear horizontal polarization (LH) of the photon beam. On the right side, the same data are compared with theoretical fits obtained with our TB model. As detailed in the Methods it comprises a total of 14 bands out of which four band pairs fall in the measurement window. The model includes orbital mixing of the 5d orbitals of Ta and the strong SOC. For clarity, we associate a specific color to each band pair. Pink, green and orange band pairs result from different linear combinations of the three  $t_{2g}$  orbitals. The first two are predicted to display mainly a  $d_{xy}$  component and a low effective mass  $m_e = 0.23m_0$  with  $m_0$  the electron mass. We note that although the green bands are not very visible here, they are clearly present on similar data taken at room temperature<sup>18</sup> and in earlier ARPES studies of KTO 2DEGs<sup>19,20</sup>, hence we include them in our model. The orange bands instead are mainly formed by mixed  $d_{xz}$  and  $d_{yz}$  orbitals and display a larger effective mass  $m_e = 0.52 m_0$ . The cyan band pair is introduced in our model as additional  $d_{xy}$  subbands originated from the quantum confinement of the carriers along the z direction. However, some uncertainty remains regarding the actual dominant orbital character (i.e.,  $d_{xy}$  or  $d_{xz/yz}$ )

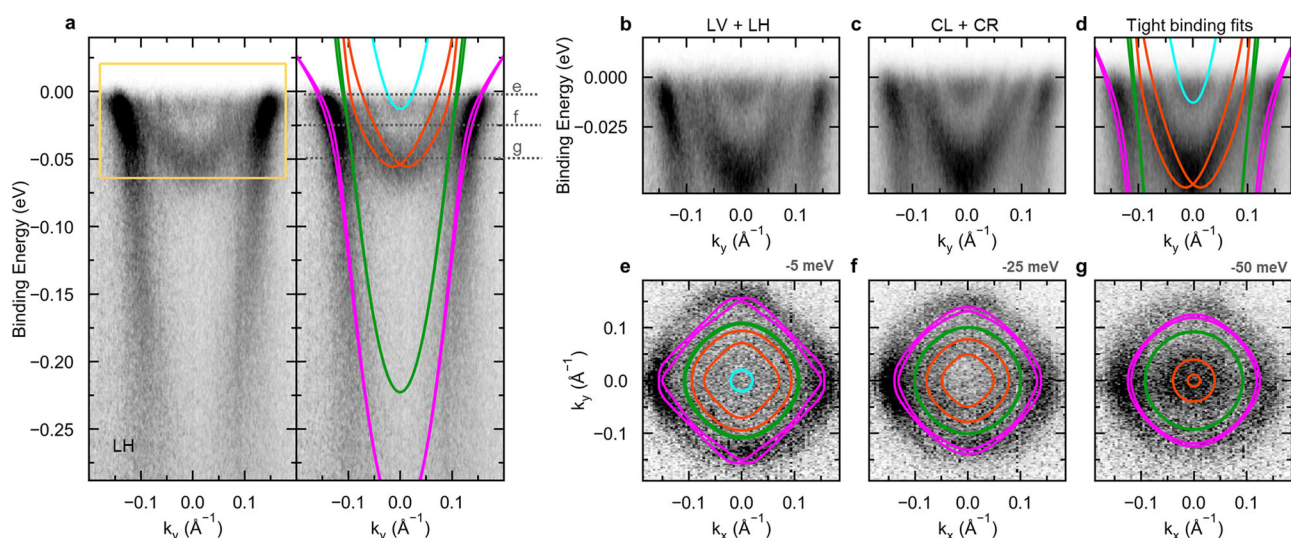


**Fig. 1 | Electronic band structure of KTO(001) 2DEGs.** **a** Band dispersion of Al/KTO(001) surface measured by ARPES. The electrons are collected at normal emission with linearly polarized photons at 31 eV ( $\Gamma_{002}$  of bulk KTO). The tight-binding fits are overlaid to the data in the right panel. A specific color is associated to each pair of bands. The yellow box highlights the energy range in panels **b–d**. **b** (**c**) Sum of

spectra obtained from two orthogonal linearly (circularly) polarized photons, i.e., linear horizontal and vertical (LV + LH), and circular left and right (CL + CR) respectively. **d** Same as **c** with overlaid tight-binding fits. Constant energy maps and theoretical contours at **e** 5 meV, **f** 25 meV and **g** 50 meV below the Fermi level. The energies are indicated by gray horizontal lines on the dispersion in panel **a**.

of this band pair. Please note that in order to describe the Rashba-like band splitting theoretically, we also had to add the  $e_g$  states  $d_{z^2}$  and the  $d_{x^2-y^2}$  to our tight-binding model, even though these states lie above the Fermi energy and are thus not observed in the ARPES measurement. By analogy with ref. 21, in Eq. (12) in the Methods section we explain that the orange band pair can be mapped to a Rashba Hamiltonian near the  $\Gamma$  point. In this effective 2-band model, the Rashba term is proportional to the orbital mixing coefficient of the  $d_{z^2}$  and the  $d_{xz/yz}$  states indicating the necessity to consider the  $e_g$  states as well.

In the measured spectra we can identify two branches close to  $\epsilon_F$ , which are nicely fitted with a visible Rashba split band pair (orange). Panels b–d display high resolution measurements to better visualize the splitting of such bands where the binding energy span corresponds to the yellow box in Fig. 1a. By symmetry,  $d_{xz}$  and  $d_{yz}$  states can be excited only with linear horizontal (LH) and vertical (LV), respectively. Thus, the complete band structure results from the sum of the LV and LH spectra (Fig. 1b). Summing circular left and right polarization (CL + CR) yields a comparable intensity distribution shown in Fig. 1c, where one can clearly appreciate two  $k$ -split bands matching with the theoretical ones (Fig. 1d).

In Fig. 1e–g, we show constant energy maps in the  $k_x k_y$  plane and the corresponding contours derived from our TB fit at binding energies of 5 meV, 25 meV and 50 meV, respectively (gray horizontal lines in panel a). The good agreement between experiment and theory validates the model and the parameters extracted from the fitting of the bands dispersion, e.g., orbital mixing, spin-orbit coupling, hopping amplitudes and on-site energies (discussed in Methods).

### Spin and orbital textures

Next, we analyse the spin and orbital textures of the 2DEG by calculating the expectation values of the spin and orbital moment operators (Eqs. (16) and (17)) using the eigenstates of the TB Hamiltonian discussed in the Methods section (Eq. (2)). Figure 2 depicts the spin and orbital textures at selected iso-energy lines. Here, we chose energies slightly above the band edge of each band pair. Near the band edge, each band pair has a Rashba-like band structure with almost circular iso-energy lines. The first (pink, Fig. 2a), second (green, Fig. 2b), and fourth (cyan, Fig. 2d) exhibit circular, Rashba-like spin and orbital textures, with the orbital moments pointing in opposite direction to the spin moments. Due to time-reversal and mirror symmetries, both textures are completely in-plane. Near the band edges, the effective Rashba parameters of these bands, characterizing the band splitting and defined by  $\alpha_R = \Delta k \hbar^2 / 2m_e$  with  $\Delta k$  the difference between the average  $k$  of the bands and  $\hbar$  the reduced Planck constant, are in the order of 10 meV  $\text{\AA}$ . The third band pair (orange) exhibits a much larger splitting, characterized by an effective Rashba parameter of approximately  $\alpha_R \approx 320$  meV  $\text{\AA}$ , which is in good agreement with values deduced from magnetotransport<sup>16,18</sup>. However and quite unexpectedly, the spin and orbital textures deviate from the pure, linear Rashba model (Fig. 2c, e). Although the orbital moments show a circular texture, their absolute values at the outer and inner bands differ and are comparably small. The spin texture deviates even more from the standard linear Rashba model. Spins have comparably small absolute values (up to  $0.09\hbar$  instead of almost  $0.5\hbar$  near the other bands' edges). Further, since the system under consideration deviates from a pure Rashba system, and the corresponding multi-band Hamiltonian also contains higher-order terms in  $k$ , the spin expectation values at

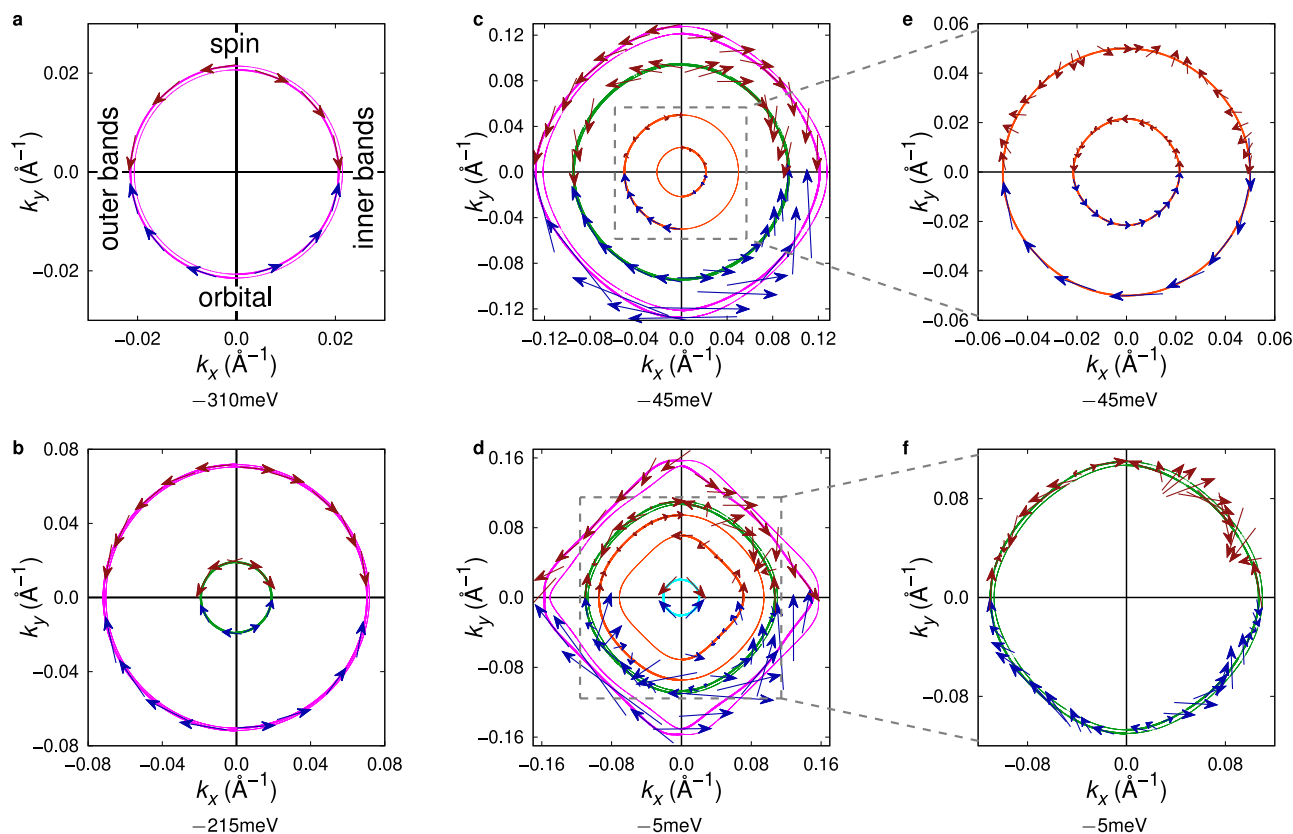


**Fig. 2 | Spin and orbital textures of electronic states.** Constant energy lines with spin and orbital textures at selected energies. Panels a–d Iso-energy lines slightly above the band edges of the four band pairs. The upper quadrants display the spin texture (red arrows), the lower quadrants the orbital expectation values (blue

arrows). Left quadrants correspond to the outer band of a pair, right quadrants to the inner band. The contours for which the spin or orbital textures are shown are drawn as slightly thicker lines. e detail of panel c. Here, all quadrants show the textures of both bands. f detail of panel d, only the second band pair (green) is shown.

the outer band perform an in-plane rotation of  $6\pi$  along the whole iso-energy line, whereas in conventional Rashba systems a  $2\pi$  rotation occurs. Due to the hybridized orbital character of approximately 50%  $d_{zx}$  and 50%  $d_{yz}$  these strongly Rashba-split bands can approximately be described by a linear Rashba Hamiltonian in the basis  $\{\frac{1}{\sqrt{2}}(|d_{zx\downarrow}\rangle + i|d_{yz\downarrow}\rangle), \frac{1}{\sqrt{2}}(|d_{zx\uparrow}\rangle - i|d_{yz\uparrow}\rangle)\}$ . However, this means that the Rashba-like texture of this band pair occurs in the pseudo spin space  $\tau = \mathbf{s}_{d_{zx}} - \mathbf{s}_{d_{yz}}$ , and not in the actual spin space  $\mathbf{s} = \mathbf{s}_{d_{zx}} + \mathbf{s}_{d_{yz}}$  which leads to a strong suppression of the spin expectation values<sup>21</sup> (more details in the Methods Section). Here,  $\mathbf{s}_{d_{zx}}$  and  $\mathbf{s}_{d_{yz}}$  are the spins of the corresponding orbitals. Also, since this band pair predominantly is formed by  $d_{zx}$  and  $d_{yz}$  states, the orbital expectation values are also strongly reduced (the corresponding matrix elements in the  $\lambda_x$  and  $\lambda_y$  matrices are zero; see Methods section).

At higher energies, the band structure deviates from the Rashba-like parabolic shape, and the iso-energy lines are no longer circles. Due to hybridization, the spin and orbital textures become more complicated. Most noticeably, their amplitudes vary along an iso-energy line (see e.g., Fig. 2d), and the amplitude of the orbital moments strongly increases at higher energies. The larger variation in the absolute values of the orbital moments in comparison to the spin expectation values can be explained qualitatively by the higher variety of the values of the corresponding quantum numbers. While there are only two possibilities of projecting the spin to a quantization axis ( $s = \frac{1}{2}$ ), there are five magnetic quantum numbers for the orbital angular momentum of the  $d$  electrons under consideration<sup>24</sup>. This larger range of magnetic quantum numbers is also reflected by stronger varying expectation values of the orbital moment. At approximately  $-26$  meV the two bands of the second band pair (green) intersect in the  $(10)$  direction, leading to unconventional textures at energies  $> -26$  meV: Fig. 2f indicates that the spin expectation values rotate by  $10\pi$  along the whole iso-energy line, and the orbital expectation values of the inner band rotate by  $6\pi$  due to deviations of the 2DEG from a pure Rashba system.

### Spin and orbital Edelstein effects

We now discuss the Edelstein effect corresponding to these bands and their spin/orbital textures. We define the Edelstein efficiency tensor  $\chi$  by the magnetic moment  $\mathbf{m}$  per 2D unit cell, induced by the electric field  $\mathbf{E}$ ,

$$\frac{A_0}{A} \mathbf{m} = \chi \mathbf{E} = (\chi^s + \chi^l) \mathbf{E}. \quad (1)$$

Here,  $A_0$  is the area of the 2D unit cell,  $A$  is the area of the sample, and  $\chi^s$  and  $\chi^l$  are the efficiencies of the spin (SEE)<sup>25</sup> and orbital Edelstein effect (OEE)<sup>26–29</sup>, respectively. The Edelstein efficiency is calculated using the semi-classical Boltzmann approach and a constant relaxation time approximation. For symmetry reasons  $\chi_{xy} = -\chi_{yx}$  are the only nonzero tensor elements. Details are discussed in the Methods Section.

Figure 3 depicts the band-resolved and total Edelstein conversion efficiency of the KTO(001) 2DEG versus the Fermi level position. Panels a and b show each band pair's contribution to the SEE and the OEE, respectively, and the total efficiencies as sum of the different pairs (red/blue). Panel c shows the total Edelstein conversion efficiency. Consistent with results on SrTiO<sub>3</sub> interfaces<sup>24</sup>, the OEE dominates the total Edelstein effect, mainly because the orbital moments are in general larger than the spin moments, and the amplitude of the orbital moments of neighboring bands differ more, as discussed above. Usually, the two bands of a pair contribute oppositely to the SEE and OEE, and their contributions partially compensate. If the expectation values differ in magnitude, this compensation is reduced, and the resulting Edelstein effect is enhanced.

When a new band pair is filled, it contributes positively or negatively to the total SEE and OEE, depending on the chirality of the corresponding moments (see Fig. 2). The fourth band pair (cyan)

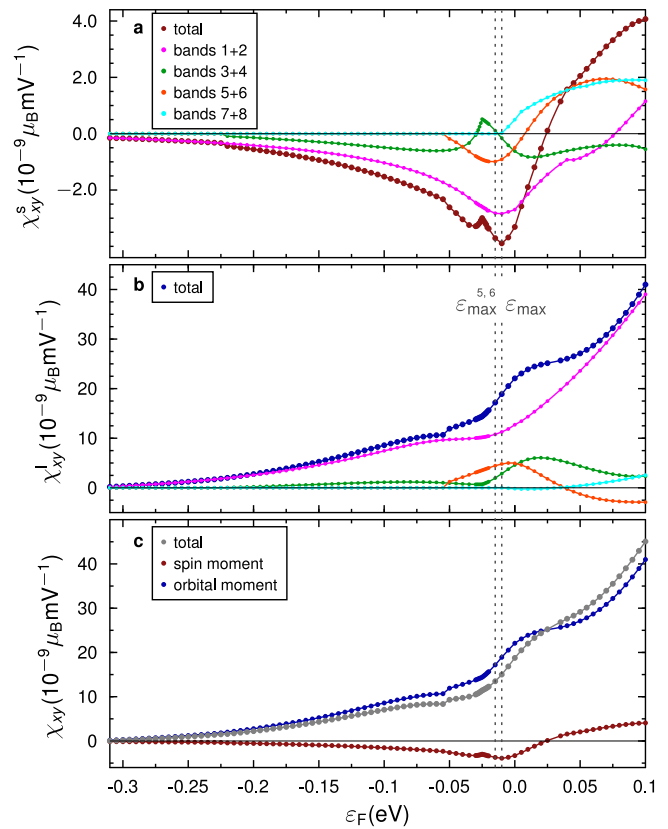


**Fig. 3 | Edelstein effect.** Edelstein conversion efficiency  $\chi_{xy}$  representing the magnetic moment per surface unit cell along  $x$  direction induced by an electric field in  $y$  direction. **a** Contribution from the spin moments (red) and contribution of each band pair (colors as in Fig. 1).  $\epsilon_{\max}$  corresponds to the energy where the total spin Edelstein efficiency is maximum,  $\epsilon_{\max}^{5,6}$  is the energy of the third band pair's (orange) maximum of the Edelstein efficiency. **b** Contribution from the orbital moments (blue) and contribution of each band pair. **c** Total Edelstein efficiency (gray).

contributes with a positive sign to the SEE, although it has the same spin chirality as the other bands. Here, the inner band's contribution dominates over the outer band's because of slightly larger spin moments, which inverts the sign of the SEE (see Fig. 2d).

At  $\epsilon = -26$  meV,  $\chi_{xy}^s$  for the second band pair (green) exhibits a sharp kink, which is also visible in the total SEE. This kink is related to the crossing of both bands of this pair, and the related strong modification of the spin texture (see Fig. 2f and discussion above).

Unexpectedly, the lowest band pair (pink) and not the strongly Rashba-split band pair (orange) dominates the SEE as well as the OEE, although the effective Rashba parameter of the latter exceeds  $\alpha_R$  of the lowest band pair by one order of magnitude. This can be directly understood by considering the spin and orbital textures of the strongly Rashba-split band pair (Fig. 2e). Since the Rashba splitting occurs in the subspace of pseudospin  $\tau$ , and not in the spin subspace (see Methods for details), the spin values are comparably small and deviate from the spin texture of a conventional Rashba system. Due to the orbital character of this band pair (mainly  $d_{zx}$  and  $d_{yz}$ ), the orbital texture is small as well. The lowest band pair (pink) has the highest density of states and therefore dominates the total SEE and OEE efficiencies. We note that the maximum spin and orbital EE found here exceed those calculated for STO 2DEGs<sup>24</sup> by a factor of  $\sim 2$  and  $\sim 4$ , respectively.

### Discussion

As discussed above, the SEE and OEE provided by the third band pair are not as large as one would expect by just considering the giant Rashba-like splitting of this band pair. For symmetry reasons, the states



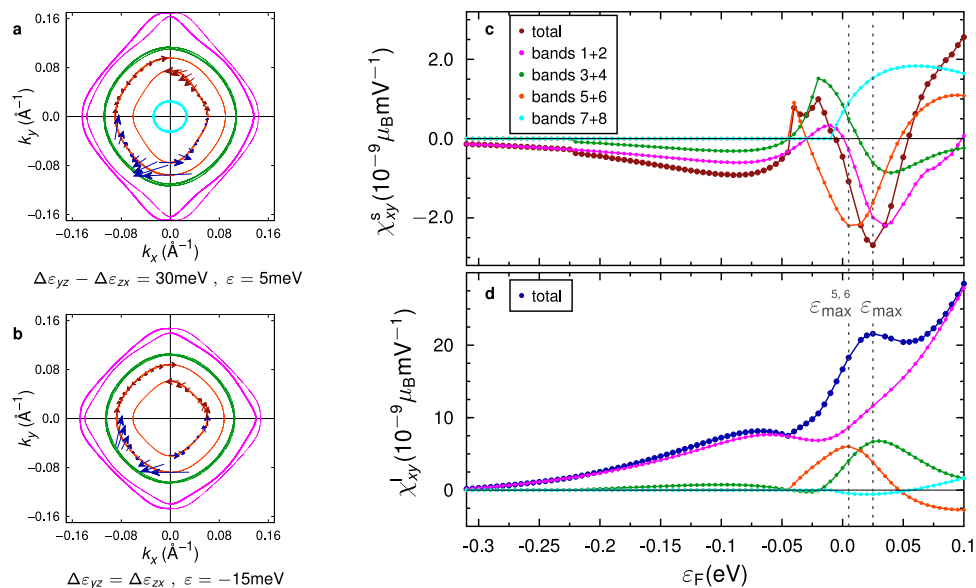


**Fig. 4 | Influence of anisotropy on the iso-energy lines and the calculated Edelstein efficiency.** **a** shows the iso-energy lines of a system with  $\Delta\epsilon_{yz} - \Delta\epsilon_{zx} = 30$  meV at  $\epsilon = 5$  meV, which corresponds to the energy of the maximum contribution of the third band pair (orange) to the spin Edelstein effect. **b** same as **a**, but for

the isotropic system (with  $\epsilon = -15$  meV the energy of the third band pair's maximum). **c** spin and **d** orbital Edelstein efficiency  $\chi_{xy}$  for an anisotropic system with  $\Delta\epsilon_{yz} - \Delta\epsilon_{zx} = 30$  meV.

of both bands have equal amount of  $d_{yz}$  and  $d_{zx}$  character, which leads to an almost complete cancellation of the spin expectation values.

In order to enhance the corresponding Edelstein efficiency, we reduce the symmetry of the system by introducing an anisotropy with respect to the  $d_{yz}$  and  $d_{zx}$  orbitals. The simplest way to simulate anisotropy in our particular model Hamiltonian is to assume different on site energies of the corresponding orbitals,  $\Delta\epsilon_{yz} \neq \Delta\epsilon_{zx}$ . In a realistic system, strain-induced anisotropy would also influence other parameters of the model, but we decided to modify only one parameter in order to demonstrate the general influence of anisotropy, and not to model details of a strained system.

Figure 4a, b show the spin and orbital textures of an anisotropic ( $\Delta\epsilon_{yz} - \Delta\epsilon_{zx} = 30$  meV) and the isotropic 2DEG, respectively. Here, we chose the energy of the third band pair's maximum contribution to the SEE (labeled  $\epsilon_{\max}^{5,6}$ ). In comparison to the isotropic system, the spin and orbital expectation values of the anisotropic system are remarkably increased, as envisaged from the low-energy expansion of the third band pair (Eq. (13)). While the character of these bands at the band edge is approximately 50% of each  $d_{yz}$  and  $d_{zx}$  in the isotropic case, this ratio strongly changes with anisotropy (62% of  $d_{zx}$  and 35% of  $d_{yz}$  for  $\Delta\epsilon_{yz} - \Delta\epsilon_{zx} = 30$  meV). Hence, the  $\mathbf{k}$  dependent spin expectation values are increased, because the contributions from both orbitals compensate less in the anisotropic case. Further, the admixture of  $d_{xy}$  states (2% at the band edges versus 0.2% in the isotropic case) leads to enhanced orbital expectation values.

Figure 4c shows the SEE and OEE efficiencies versus the Fermi level for an anisotropic system with  $\Delta\epsilon_{yz} - \Delta\epsilon_{zx} = 30$  meV. In comparison to the SEE and OEE in the isotropic case (Fig. 3), the contribution of the third band pair (orange) to the total SEE and OEE signal is indeed increased by a factor  $\sim 3$  due to the enhanced  $\mathbf{k}$  dependent spin and orbital expectation values. However, the anisotropy also affects the other band pairs, and the total SEE and OEE, which are superpositions of all bands' contributions, are reduced. Obviously, the Edelstein tensor becomes anisotropic in the presence of strain,  $\chi_{xy} \neq -\chi_{yx}$ , and in general the magnitude of  $\chi_{xy}$  and  $\chi_{yx}$  are affected oppositely by anisotropy.

Our work shows that even when the host material contains a heavy element such as Ta, in 2DEGs based on  $d$  element perovskite

oxides and accordingly displaying a substantial Rashba splitting, the orbital symmetry may lead to strong compensation effects, limiting the spin-charge interconversion efficiency through the EE and inverse EE. The compensation effects are three-fold: (i) the EE from the  $d_{xz/yz}$  band is weaker than expected due to the opposite spin textures of  $d_{xz}$  and  $d_{yz}$  components; (ii) the EE from the  $d_{xy}$  bands and  $d_{xz/yz}$  bands typically have opposite sign; (iii) the spin EE and orbital EE generally have opposite signs, the total response being dominated by the orbital EE.

Our calculations indicate that introducing in-plane anisotropy is necessary to unleash the potential of the  $d_{xz/yz}$  Rashba split bands for spin-charge interconversion in KTO 2DEGs. This can be achieved from a cubic material like KTO by making it orthorhombic, e.g., by growing it on orthorhombic substrates such as rare-earth scandates which have a good lattice match with KTO. Another approach to lift the  $d_{xz/yz}$  orbital degeneracy is to design a 2DEG from a material that, unlike KTO, is orthorhombic in the bulk. Candidates include SrZrO<sub>3</sub>, CaZrO<sub>3</sub> or CaHfO<sub>3</sub>. DFT simulations predict that this latter compound, that includes the  $5d$  element Hf, can be made metallic through doping with oxygen vacancies<sup>30</sup>, similar to STO and KTO, which suggests that it may host a 2DEG when interfaced with another oxide.

To suppress the second compensation effect, it may be attractive to generate 2DEGs in oxide materials in which crystal field splitting causes the  $d_{xz/yz}$  bands to lie below the  $d_{xy}$  bands. Recent ARPES measurements suggested that such a band order inversion occurs at interfaces between STO and  $\gamma$ -Al<sub>2</sub>O<sub>3</sub><sup>31</sup>. It would be interesting to see if the same inversion could be engineered in KTO 2DEGs. We note that in anatase TiO<sub>2</sub>, which was shown to be a suitable 2DEG host<sup>32</sup>, the  $d_{xz/yz}$  bands also lie below the  $d_{xy}$  bands. This material and related members of its family, if properly engineered, thus look promising for efficient spin-charge interconversion by EE and inverse EE.

Finally, although this is not true at all energies, in KTO 2DEGs the spin EE and the orbital EE typically compete with each other. In classical spin pumping experiments only a spin current is injected and the conversion to a charge current is mostly driven by the spin EE<sup>8</sup>. However, in more advanced schemes aiming to harness orbital-charge interconversion as well<sup>33</sup> it would be beneficial to work with

systems in which the spin EE and orbital EE have the same sign. Materials with more than half-filled orbitals, in which the spin and orbital moments should be parallel, could represent a fruitful research direction.

## Methods

### Sample preparation

After preannealing the KTO at 300 °C for 1 h in UHV, we grew 1–2 Å of Al at room temperature at  $7 \times 10^{-10}$  mbar using a Knudsen cell heated to 1000 °C at a growth rate of  $0.011 \text{ \AA} \cdot \text{s}^{-1}$ . The samples were then transferred in UHV to the connected ARPES chamber. Low-energy electron diffraction performed on the samples before and after Al deposition showed sharp diffraction spots corresponding to a square lattice, attesting to the high structural coherence of the surface. In situ X-ray photoelectron spectroscopy showed that Al deposition onto KTO led to the reduction of the Ta valence from the nominal 5+, consistent with 2DEG formation<sup>18</sup>, and that Al was fully oxidized to Al<sup>3+</sup>.

### Angular resolved photoemission spectroscopy

High resolution angular resolved photoemission spectroscopy (ARPES) spectra were collected at the Cassiopée beamline of Synchrotron SOLEIL (France), by a Scienta R4000 electron energy analyser. The beamline allows to control the energy and polarization of the VUV photons. Data presented in the manuscript were collected at different polarization to probe electron states with different orbital symmetries: linear horizontal (i.e., parallel) or vertical (i.e. perpendicular) to the scattering plane (LH or LV), and circular left or right (CL or CR). Considering the sample surface plane  $xy$ , for a normal emission geometry the scattering plane is defined as the mirror plane  $xz$ . Using vertical polarization (LV) allows to probe only odd symmetry orbitals with respect to  $xz$  plane, corresponding to  $d_{xy}$  and  $d_{yz}$  orbitals. By using horizontal slit (LH), only  $d_{xz}$  orbitals are selected. The sum of the LH and LV spectra would thus contain contribution from all the  $e_g$  bands. The sample was kept at 15 K by liquid He in order to minimize the thermal noise. The energy and angular resolution were 15 meV and  $<0.25^\circ$ .

### Tight-binding model

We diagonalize the tight-binding Hamiltonian

$$H = H_{\text{hop}} + H_{\text{SOC}} + H_{\text{mix}} \quad (2)$$

to describe the electron gas that is confined at the interface. In the model, the electron gas consists of a single layer square lattice (lattice constant  $a = 4.0 \text{ \AA}$ ) formed by the Ta atoms. Only the  $5d$  electrons of the Ta atoms have been considered, since they form the states close to the Fermi energy. The model is similar to our previous works on STO 2DEGs<sup>8,24</sup> but instead of considering only the three  $t_{2g}$  orbitals, we also consider the  $d_{z^2}$  and  $d_{x^2-y^2}$  orbitals. For the  $d_{xy}$  orbital we consider two additional subbands. In total, the Hamiltonian is a  $14 \times 14$  matrix which results in 14 bands in the band structure. The basis is

$$\{ |d_{z^2\uparrow}\rangle, |d_{z^2\downarrow}\rangle, |d_{x^2-y^2\uparrow}\rangle, |d_{x^2-y^2\downarrow}\rangle, |d_{xy1\uparrow}\rangle, |d_{xy1\downarrow}\rangle, |d_{xy2\uparrow}\rangle, |d_{xy2\downarrow}\rangle, |d_{xy3\uparrow}\rangle, |d_{xy3\downarrow}\rangle, |d_{zx\uparrow}\rangle, |d_{zx\downarrow}\rangle, |d_{yz\uparrow}\rangle, |d_{yz\downarrow}\rangle \}. \quad (3)$$

Since we consider a two-dimensional system with hoppings along  $x$  and  $y$ , the hopping matrix  $H_{\text{hop}}$  is diagonal except for a mixing of  $d_{z^2}$

and  $d_{x^2-y^2}$  states

$$H_{\text{hop}} = \begin{pmatrix} \epsilon_{z^2} & m_{z^2,x^2-y^2} & 0 & 0 & 0 & 0 & 0 \\ m_{z^2,x^2-y^2} & \epsilon_{x^2-y^2} & 0 & 0 & 0 & 0 & 0 \\ 0 & 0 & \epsilon_{xy1} & 0 & 0 & 0 & 0 \\ 0 & 0 & 0 & \epsilon_{xy2} & 0 & 0 & 0 \\ 0 & 0 & 0 & 0 & \epsilon_{xy3} & 0 & 0 \\ 0 & 0 & 0 & 0 & 0 & \epsilon_{zx} & 0 \\ 0 & 0 & 0 & 0 & 0 & 0 & \epsilon_{yz} \end{pmatrix} \otimes \begin{pmatrix} 1 & 0 \\ 0 & 1 \end{pmatrix} \quad (4)$$

The elements of this matrix have been determined by using the Slater–Koster formalism

$$\epsilon_{z^2} = \frac{t_\sigma + 3t_\delta}{2} [\cos(ak_x) + \cos(ak_y)] + \Delta\epsilon_{z^2} \quad (5)$$

$$\epsilon_{x^2-y^2} = \frac{3t_\sigma + t_\delta}{2} [\cos(ak_x) + \cos(ak_y)] + \Delta\epsilon_{x^2-y^2} \quad (6)$$

$$\epsilon_{xy(1,2,3)} = 2t_\pi \cos(ak_x) + 2t_\pi \cos(ak_y) + \Delta\epsilon_{xy(1,2,3)} \quad (7)$$

$$\epsilon_{zx} = 2t_\pi \cos(ak_x) + 2t_\delta \cos(ak_y) + \Delta\epsilon_{zx} \quad (8)$$

$$\epsilon_{yz} = 2t_\delta \cos(ak_x) + 2t_\pi \cos(ak_y) + \Delta\epsilon_{yz} \quad (9)$$

$$m_{z^2,x^2-y^2} = \frac{\sqrt{3}}{2} (t_\delta - t_\sigma) [\cos(ak_x) - \cos(ak_y)] \quad (10)$$

Independent hopping amplitudes are  $t_\sigma = -0.46 \text{ eV}$ ,  $t_\pi = -1.37 \text{ eV}$  and  $t_\delta = -0.07 \text{ eV}$ . To account for the band shift due to the broken inversion symmetry at the interface, we take into account the onsite-energies  $\Delta\epsilon_{z^2} = 3.670 \text{ eV}$ ,  $\Delta\epsilon_{x^2-y^2} = 21.45 \text{ eV}$ ,  $\Delta\epsilon_{xy1} = 5.180 \text{ eV}$ ,  $\Delta\epsilon_{xy2} = 5.275 \text{ eV}$ ,  $\Delta\epsilon_{xy3} = 5.515 \text{ eV}$ ,  $\Delta\epsilon_{zx} = 2.885 \text{ eV}$  and  $\Delta\epsilon_{yz} = 2.885 \text{ eV}$ .

The matrix  $H_{\text{SOC}}$  with  $\lambda = 0.16 \text{ eV}$  describes on-site spin-orbit coupling and mixes different spins and even different orbital

$$H_{\text{SOC}} = \frac{2}{3}\lambda \begin{pmatrix} 0 & 0 & 0 & 0 & 0 & 0 & 0 & 0 & 0 & 0 & 0 & -\frac{\sqrt{3}}{2} & 0 & i\frac{\sqrt{3}}{2} \\ 0 & 0 & 0 & 0 & 0 & 0 & 0 & 0 & 0 & 0 & 0 & \frac{\sqrt{3}}{2} & 0 & i\frac{\sqrt{3}}{2} \\ 0 & 0 & 0 & 0 & -i & 0 & -i & 0 & -i & 0 & 0 & \frac{1}{2} & 0 & \frac{i}{2} \\ 0 & 0 & 0 & 0 & 0 & i & 0 & i & 0 & i & -\frac{1}{2} & 0 & \frac{i}{2} & 0 \\ 0 & 0 & i & 0 & 0 & 0 & 0 & 0 & 0 & 0 & 0 & -\frac{i}{2} & 0 & \frac{1}{2} \\ 0 & 0 & 0 & -i & 0 & 0 & 0 & 0 & 0 & 0 & -\frac{i}{2} & 0 & -\frac{1}{2} & 0 \\ 0 & 0 & 0 & 0 & 0 & 0 & 0 & 0 & 0 & 0 & 0 & -\frac{i}{2} & 0 & \frac{1}{2} \\ 0 & 0 & 0 & -i & 0 & 0 & 0 & 0 & 0 & 0 & -\frac{i}{2} & 0 & -\frac{1}{2} & 0 \\ 0 & 0 & i & 0 & 0 & 0 & 0 & 0 & 0 & 0 & -\frac{i}{2} & 0 & \frac{1}{2} & 0 \\ 0 & 0 & 0 & -i & 0 & 0 & 0 & 0 & 0 & 0 & -\frac{i}{2} & 0 & -\frac{1}{2} & 0 \\ 0 & \frac{\sqrt{3}}{2} & 0 & -\frac{1}{2} & 0 & \frac{i}{2} & 0 & \frac{i}{2} & 0 & \frac{i}{2} & 0 & 0 & -\frac{i}{2} & 0 \\ -\frac{\sqrt{3}}{2} & 0 & \frac{1}{2} & 0 & \frac{i}{2} & 0 & \frac{i}{2} & 0 & \frac{i}{2} & 0 & 0 & 0 & 0 & \frac{i}{2} \\ 0 & -i\frac{\sqrt{3}}{2} & 0 & -\frac{i}{2} & 0 & -\frac{1}{2} & 0 & -\frac{1}{2} & 0 & -\frac{1}{2} & \frac{i}{2} & 0 & 0 & 0 \\ -i\frac{\sqrt{3}}{2} & 0 & -\frac{i}{2} & 0 & \frac{1}{2} & 0 & \frac{1}{2} & 0 & \frac{1}{2} & 0 & 0 & -\frac{i}{2} & 0 & 0 \end{pmatrix} \quad (11)$$

Due to the gradient potential at the interface, the oxygen  $p$  orbitals are displaced away from the bond connecting two Ta atoms. This allows for hopping terms that are forbidden in the bulk. The effective hopping amplitude in a hopping network between two neighboring Ta  $d$  orbitals, via an intermediate hopping to a oxygen  $p$  orbital, is finite and antisymmetric<sup>34,35</sup> when mixing  $d_{zx}$  or  $d_{yz}$  with  $d_{xy}$ ,  $d_{z^2}$  or  $d_{x^2-y^2}$  orbitals. This gives rise to ref. 21

$$H_{\text{mix}} = 2i \begin{pmatrix} 0 & 0 & 0 & 0 & 0 & -g_2 \sin(ak_x) & -g_2 \sin(ak_y) \\ 0 & 0 & 0 & 0 & 0 & -g_3 \sin(ak_x) & g_3 \sin(ak_y) \\ 0 & 0 & 0 & 0 & 0 & g_1 \sin(ak_y) & g_1 \sin(ak_x) \\ 0 & 0 & 0 & 0 & 0 & g_1 \sin(ak_y) & g_1 \sin(ak_x) \\ 0 & 0 & 0 & 0 & 0 & g_1 \sin(ak_y) & g_1 \sin(ak_x) \\ g_2 \sin(ak_x) & g_3 \sin(ak_x) & -g_1 \sin(ak_y) & -g_1 \sin(ak_y) & -g_1 \sin(ak_y) & 0 & 0 \\ g_2 \sin(ak_y) & -g_3 \sin(ak_y) & -g_1 \sin(ak_x) & -g_1 \sin(ak_x) & -g_1 \sin(ak_x) & 0 & 0 \end{pmatrix} \otimes \begin{pmatrix} 1 & 0 \\ 0 & 1 \end{pmatrix} \quad (12)$$

with the amplitudes  $g_1 = 0.005 \text{ eV}$ ,  $g_2 = 0.5 \text{ eV}$  and  $g_3 = 0.002 \text{ eV}$ .

Note that we did not observe the  $d_{x^2-y^2}$  and  $d_{z^2}$  bands in the ARPES measurements, as they are several eV above the Fermi energy. On the one hand, considering the  $d_{x^2-y^2}$  orbital was not useful for improving the fit which is why we practically disregarded this band pair by using a large onsite energy  $\Delta\epsilon_{x^2-y^2}$ . Still, we wanted to include this orbital for the sake of completeness. On the other hand, considering  $d_{z^2}$  improved the fit significantly. In fact, without this orbital we were not able to reproduce the large Rashba splitting of the lower  $d_{zx/yz}$  bands. The origin of this effect has been explained in ref. 21 for a monolayer of BaHfO<sub>3</sub>: Near  $\Gamma$  the Hamiltonian can be expanded in  $\mathbf{k}$ . For the band pair with the strong Rashba splitting (the lower  $d_{zx/yz}$  bands), we get

$$H_{\text{eff}} = h(\mathbf{k}) \begin{pmatrix} 1 & 0 \\ 0 & 1 \end{pmatrix} + \frac{2\sqrt{3}g_2\lambda}{\epsilon_{z^2} - \epsilon_{yz/zx}} (\boldsymbol{\tau} \times \mathbf{k}) \cdot \mathbf{e}_z, \quad (13)$$

if we treat these two bands individually in the basis  $\{\frac{1}{\sqrt{2}}(|d_{zx\downarrow}\rangle + i|d_{yz\downarrow}\rangle), \frac{1}{\sqrt{2}}(|d_{zx\uparrow}\rangle - i|d_{yz\uparrow}\rangle)\}$ . The second term describes the Rashba splitting. It is quantified by  $g_2$  (the orbital mixing amplitude of  $d_{z^2}$  with  $d_{yz}$  and  $d_{zx}$ ), as well as by  $\epsilon_{z^2} - \epsilon_{yz/zx}$  (the energy difference of the  $d_{yz}/d_{zx}$  band pair and the  $d_{z^2}$  band at the  $\Gamma$  point).  $\boldsymbol{\tau}$  describes the pseudo spin  $\boldsymbol{\tau} = \mathbf{s}_{d_{zx}} - \mathbf{s}_{d_{yz}}$  which forms a Rashba spin texture on the Fermi line. However, the actual spin  $\mathbf{s} = \mathbf{s}_{d_{zx}} + \mathbf{s}_{d_{yz}}$  is compensated. This explains why the spin texture of the band pair with the strong Rashba splitting is so small in the full model.

### Calculation of the spin and orbital Edelstein effect

We use the semiclassical Boltzman transport theory to calculate the spin and orbital Edelstein efficiencies defined by Eq. (1). The magnetization  $\mathbf{m}_{s/l}$  originating from the spin and orbital moments, respectively, and induced by the external electric field  $\mathbf{E}$  is calculated as ref. 24

$$\mathbf{m}_{s/l} = -\frac{g_{s/l}\mu_B}{h} \sum_{\mathbf{k}} f_{\mathbf{k}} \langle \mathbf{s}/\mathbf{l} \rangle_{\mathbf{k}}. \quad (14)$$

Here,  $g_{s/l}$  are the spin and orbital Landé's  $g$  factors, respectively, which we have set to  $g_s = 2$  and  $g_l = 1$  in our calculations.  $\mu_B$  is the Bohr magneton,  $f_{\mathbf{k}}$  is the distribution function, and  $\langle \mathbf{s}/\mathbf{l} \rangle_{\mathbf{k}}$  is the  $\mathbf{k}$  dependent expectation value of the spin and orbital moment, respectively, which is calculated by

$$\langle \mathbf{s}/\mathbf{l} \rangle_{\mathbf{k}} = \langle \Psi_{\mathbf{k}} | \mathbf{s}/\mathbf{l} | \Psi_{\mathbf{k}} \rangle. \quad (15)$$

$|\Psi_{\mathbf{k}}\rangle$  are the eigenstates of the Hamiltonian Eq. (2). For reasons of clearness, we have merged the crystal momentum  $\hbar\mathbf{k}$  and the band index  $n$  to the multi-index  $\mathbf{k}$  here and in the following. The operators of spin and orbital moment in the basis Eq. (3) of the tight-binding Hamiltonian Eq. (2) are

$$\mathbf{s} = \frac{\hbar}{2} \mathbb{1}_7 \otimes \boldsymbol{\sigma}, \mathbf{l} = \hbar \boldsymbol{\lambda} \otimes \mathbb{1}_2 \quad (16)$$

with

$$\lambda_x = \begin{pmatrix} 0 & 0 & 0 & 0 & 0 & 0 & \sqrt{3}i \\ 0 & 0 & 0 & 0 & 0 & 0 & i \\ 0 & 0 & 0 & 0 & 0 & -i & 0 \\ 0 & 0 & 0 & 0 & 0 & -i & 0 \\ 0 & 0 & 0 & 0 & 0 & -i & 0 \\ 0 & 0 & 0 & i & i & 0 & 0 \\ -\sqrt{3}i & -i & 0 & 0 & 0 & 0 & 0 \end{pmatrix}, \lambda_y = \begin{pmatrix} 0 & 0 & 0 & 0 & 0 & -\sqrt{3}i & 0 \\ 0 & 0 & 0 & 0 & 0 & i & 0 \\ 0 & 0 & 0 & 0 & 0 & 0 & i \\ 0 & 0 & 0 & 0 & 0 & 0 & i \\ 0 & 0 & 0 & 0 & 0 & 0 & i \\ \sqrt{3}i & -i & 0 & 0 & 0 & 0 & 0 \\ 0 & 0 & -i & -i & -i & 0 & 0 \end{pmatrix},$$

$$\lambda_z = \begin{pmatrix} 0 & 0 & 0 & 0 & 0 & 0 & 0 \\ 0 & 0 & -2i & -2i & -2i & 0 & 0 \\ 0 & 2i & 0 & 0 & 0 & 0 & 0 \\ 0 & 2i & 0 & 0 & 0 & 0 & 0 \\ 0 & 2i & 0 & 0 & 0 & 0 & 0 \\ 0 & 0 & 0 & 0 & 0 & 0 & -i \\ 0 & 0 & 0 & 0 & 0 & i & 0 \end{pmatrix} \quad (17)$$

Here,  $\mathbb{1}_m$  is the  $m \times m$  unity matrix.

The distribution function  $f_{\mathbf{k}}$  is calculated by solving the semi-classical Boltzmann equation for a stationary and spatially homogeneous system,

$$\mathbf{k} \cdot \frac{\partial f_{\mathbf{k}}}{\partial \mathbf{k}} = \left( \frac{\partial f_{\mathbf{k}}}{\partial t} \right)_{\text{scatt}} \quad (18)$$

The left-hand side corresponds to the influence of external fields on the distribution function. In the presence of an external electric field  $\mathbf{E}$ , it is given by the semiclassical equation of motion

$$\dot{\mathbf{k}} = -\frac{e}{\hbar} \mathbf{E} \quad (19)$$

with  $e$  the absolute value of the elementary charge. The right-hand side of Eq. (18) corresponds to the scattering term. Using the constant relaxation time approximation

$$\left( \frac{\partial f_{\mathbf{k}}}{\partial t} \right)_{\text{scatt}} = -\frac{1}{\tau_0} (f_{\mathbf{k}} - f_{\mathbf{k}}^0) \quad (20)$$

with  $\tau_0$  the constant momentum relaxation time (set to  $\tau_0 = 1 \text{ ps}$  in our calculations) and  $f_{\mathbf{k}}^0$  the equilibrium distribution function (which is the Fermi Dirac distribution function for fermions), the Boltzmann Eq. (18) is solved by

$$f_{\mathbf{k}} = f_{\mathbf{k}}^0 + \frac{\partial f_{\mathbf{k}}^0}{\partial \epsilon} e\tau_0 \mathbf{v}_{\mathbf{k}} \cdot \mathbf{E}. \quad (21)$$

The group velocity  $\mathbf{v}_{\mathbf{k}}$  is the expectation value of the velocity operator  $\hat{\mathbf{v}}$ ,

$$\mathbf{v}_{\mathbf{k}} = \langle \Psi_{\mathbf{k}} | \hat{\mathbf{v}} | \Psi_{\mathbf{k}} \rangle \quad (22)$$

with  $\hat{\mathbf{v}} = i/\hbar [H, \hat{\mathbf{r}}] = 1/\hbar \partial H / \partial \mathbf{k}$  and  $\hat{\mathbf{r}} = i\partial / \partial \mathbf{k}$ .

## Data availability

The data from Figs. 1–4 are respectively available at: <https://zenodo.org/record/7051384#.YxZTNH7BziU>, <https://zenodo.org/record/7058713#.Yxmv1GHP1H4>, <https://zenodo.org/record/7058758#.Yxmv12HP1H4>, <https://zenodo.org/record/7058806#.Yxmvx2HP1H4>.

## Code availability

The in-house code used to produced data in Figs. 1–4 is available from the authors upon reasonable request.

## References

- Bychkov, Y. A. & Rashba, E. I. Properties of a 2D electron gas with lifted spectral degeneracy. *JETP Lett.* **39**, 78 (1984).
- Manchon, A., Koo, H. C., Nitta, J., Frolov, S. M. & Duine, R. A. New perspectives for Rashba spin-orbit coupling. *Nat. Mater.* **14**, 871–882 (2015).
- LaShell, S., McDougall, B. A. & Jensen, E. Spin splitting of an Au(111) surface state band observed with angle resolved photoelectron spectroscopy. *Phys. Rev. Lett.* **77**, 3419–3422 (1996).
- Varykhalov, A. et al. Ir(111) surface state with giant rashba splitting persists under graphene in air. *Phys. Rev. Lett.* **108**, 066804 (2012).
- Ast, C. R. et al. Giant spin splitting through surface alloying. *Phys. Rev. Lett.* **98**, 186807 (2007).
- Rojas-Sánchez, J. C. et al. Spin-to-charge conversion using Rashba coupling at the interface between non-magnetic materials. *Nat. Commun.* **4**, 2944 (2013).
- Lesne, E. et al. Highly efficient and tunable spin-to-charge conversion through Rashba coupling at oxide interfaces. *Nat. Mater.* **15**, 1261 (2016).
- Vaz, D. C. et al. Mapping spin-charge conversion to the band structure in a topological oxide two-dimensional electron gas. *Nat. Mater.* **18**, 1187–1193 (2019).
- Ohtomo, A. & Hwang, H. Y. A high-mobility electron gas at the LaAlO<sub>3</sub>/SrTiO<sub>3</sub> heterointerface. *Nature* **427**, 423–426 (2004).
- Caviglia, A. D. et al. Tunable Rashba Spin-Orbit Interaction at Oxide Interfaces. *Phys. Rev. Lett.* **104**, 126803 (2010).
- Vaz, D. C. et al. Determining the Rashba parameter from the bilinear magnetoresistance response in a two-dimensional electron gas. *Phys. Rev. Mater.* **4**, 071001 (2020).
- Santander-Syro, A. F. et al. Giant spin splitting of the two-dimensional electron gas at the surface of SrTiO<sub>3</sub>. *Nat. Mater.* **13**, 1085–1090 (2014).
- McKeown Walker, S. et al. Absence of giant spin splitting in the two-dimensional electron liquid at the surface of srTiO<sub>3</sub> (001). *Phys. Rev. B* **93**, 245143 (2016).
- Gupta, A. et al. KTaO<sub>3</sub>—the new kid on the spintronics block. *Adv. Mater.* **34**, 2106481 (2022).
- Wemple, S. H. Some transport properties of oxygen-deficient single-crystal potassium tantalate (KTaO<sub>3</sub>). *Phys. Rev.* **137**, A1575–A1582 (1965).
- Zhang, H. et al. Unusual electric and optical tuning of KTaO<sub>3</sub>—based two-dimensional electron gases with 5d orbitals. *ACS Nano* **13**, 609–615 (2019).
- Wadehra, N. et al. Planar Hall effect and anisotropic magnetoresistance in polar-polar interface of LaVO<sub>3</sub>-KTaO<sub>3</sub> with strong spin-orbit coupling. *Nat. Commun.* **11**, 874 (2020).
- Vicente-Arche, L. M. et al. Spin-charge interconversion in KTaO<sub>3</sub> 2d electron gases. *Adv. Mater.* **33**, 2102102 (2021).
- Santander-Syro, A. F. et al. Orbital symmetry reconstruction and strong mass renormalization in the two-dimensional electron gas at the surface of KTaO<sub>3</sub>. *Phys. Rev. B* **86**, 121107 (2012).
- King, P. D. C. et al. Subband structure of a two-dimensional electron gas formed at the polar surface of the strong spin-orbit perovskite KTaO<sub>3</sub>. *Phys. Rev. Lett.* **108**, 117602 (2012).
- Kim, M., Ihm, J. & Chung, S. B. Strongly enhanced rashba splittings in an oxide heterostructure: A tantalate monolayer on BaHfO<sub>3</sub>. *Phys. Rev. B* **94**, 115431 (2016).
- Sunko, V. et al. Maximal Rashba-like spin splitting via kinetic-energy-coupled inversion-symmetry breaking. *Nature* **549**, 492–496 (2017).
- Rödel, T. C. et al. Universal Fabrication of 2D Electron Systems in Functional Oxides. *Adv. Mater.* **28**, 1976–1980 (2016).
- Johansson, A., Göbel, B., Henk, J., Bibes, M. & Mertig, I. Spin and orbital Edelstein effects in a two-dimensional electron gas: Theory and application to SrTiO<sub>3</sub> interfaces. *Phys. Rev. Res.* **3**, 013275 (2021).
- Edelstein, V. Spin polarization of conduction electrons induced by electric current in two-dimensional asymmetric electron systems. *Sol. State Commun.* **73**, 233–235 (1990).
- Levitov, L. S. & Nazarov, Y. V. Magnetoelectric effects in conductors with mirror isomer symmetry. *Sov. Phys. JETP* **61**, 133 (1985).
- Yoda, T., Yokoyama, T. & Murakami, S. Current-induced Orbital and Spin Magnetizations in Crystals with Helical Structure. *Sci. Rep.* **5**, 12024 (2015).
- Go, D. et al. Toward surface orbitronics: giant orbital magnetism from the orbital Rashba effect at the surface of sp-metals. *Sci. Rep.* **7**, 46742 (2017).
- Salemi, L., Berritta, M., Nandy, A. K. & Oppeneer, P. M. Orbitaly dominated Rashba-Edelstein effect in noncentrosymmetric anti-ferromagnets. *Nat. Commun.* **10**, 5381 (2019).
- Alay-e Abbas, S. M., Nazir, S., Mun Wong, K., Shaikat, A. & Schwingenschlögl, U. Chemical stability and defect formation in CaHfO<sub>3</sub>. *Europhys. Lett.* **106**, 27003 (2014).
- Chikina, A. et al. Band-order anomaly at the  $\gamma$ -Al<sub>2</sub>O<sub>3</sub>/SrTiO<sub>3</sub> interface drives the electron-mobility boost. *ACS Nano* **15**, 4347–4356 (2021).
- Sarkar, T. et al. Electron transport at the TiO<sub>2</sub> surfaces of rutile, anatase, and strontium titanate: the influence of orbital corrugation. *ACS Appl. Mater. Interfaces* **7**, 24616–24621 (2015).
- Go, D., Jo, D., Lee, H.-W., Kläui, M. & Mokrousov, Y. Orbitronics: Orbital currents in solids. *EPL (Europhys. Lett.)* **135**, 37001 (2021).
- Khalsa, G., Lee, B. & MacDonald, A. H. Theory of t<sub>2g</sub> electron-gas rashba interactions. *Phys. Rev. B* **88**, 041302 (2013).
- Zhong, Z., Tóth, A. & Held, K. Theory of spin-orbit coupling at LaAlO<sub>3</sub>/SrTiO<sub>3</sub> interfaces and srTiO<sub>3</sub> surfaces. *Phys. Rev. B* **87**, 161102 (2013).

## Acknowledgements

This project received funding from the ERC Advanced Grant “FRESCO” (#833973), the QuantERA project “QUANTOX” (ANR-18-QUAN-0014), the French ANR projects “QUANTOP” (ANR-19-CE47-0006-01) and “CORN-FLAKE” (ANR-18-CE24-0015-01), and Intel’s Science Technology Center - FEINMAN. M.B. thanks the Alexander von Humboldt Foundation for supporting his stays at Martin-Luther-Universität Halle. The authors thank J.-P. Attané, L. Vila, C. Proust and D. Vignolles for useful discussions.

## Author contributions

M.B. proposed the study and led it with I.M. L.M.V.A. prepared the samples with help from J.R. and P.L. S.V. led the ARPES study with S.M. and L.M.V.A., with support from J.B., R.S., J.R., F.B., and P.L. S.V. analysed the ARPES data and discussed them with A.J., B.G., L.M.V.A., S.M., J.B., N.B., I.M., and M.B. B.G. performed the TB fits with help from A.J. and I.M. A.J. performed the EE calculations with help from B.G. and I.M. M.B., S.V., A.J., and B.G. wrote the paper with inputs from all authors.



## Competing interests

The authors declare no competing interests.

## Additional information

**Correspondence** and requests for materials should be addressed to Annika Johansson or Manuel Bibes.

**Peer review information** *Nature Communications* thanks M. Rubhausen and the other anonymous reviewer(s) for their contribution to the peer review of this work.

**Reprints and permission information** is available at <http://www.nature.com/reprints>

**Publisher's note** Springer Nature remains neutral with regard to jurisdictional claims in published maps and institutional affiliations.

**Open Access** This article is licensed under a Creative Commons Attribution 4.0 International License, which permits use, sharing, adaptation, distribution and reproduction in any medium or format, as long as you give appropriate credit to the original author(s) and the source, provide a link to the Creative Commons license, and indicate if changes were made. The images or other third party material in this article are included in the article's Creative Commons license, unless indicated otherwise in a credit line to the material. If material is not included in the article's Creative Commons license and your intended use is not permitted by statutory regulation or exceeds the permitted use, you will need to obtain permission directly from the copyright holder. To view a copy of this license, visit <http://creativecommons.org/licenses/by/4.0/>.

© The Author(s) 2022